Welding in the World (2020) 64:1597–1604
https://doi.org/10.1007/s40194-020-00944-w

RESEARCH PAPER

Application of the eutectic high entropy alloy $Nb_{0.73}CoCrFeNi_{2.1}$ for high temperature joints

W. Tillmann[1] · L. Wojarski[1] · D. Stangier[1] · M. Manka[1] · C. Timmer[1]

Received: 5 May 2019 / Accepted: 15 June 2020 / Published online: 6 July 2020

Abstract

The eutectic high entropy alloy Nb0.73CoCrFeNi2.1 was manufactured by means of arc smelting and the obtained ingots were cut into 300-μm-thick foils, which were used as filler alloys to braze Crofer 22 APU to Hf-metallized yttria-stabilized zirconia (3YSZ). The brazing process was conducted in a vacuum furnace at 1200 °C for 5 min at a vacuum of 4.3·10–4 mbar. In order to minimize the intense diffusion and erosion of the steel substrate, a heating and cooling rate of 50 K/min was applied. Sound joints without any pores or flaws were obtained. The microstructure of the joints consisted of an HfO2 reaction layer at the ceramic interface and the same eutectic structure consisting of a Laves phase and a solid solution that was already detected in the smelted foil. The average hardness of the microstructure in the joint seam amounted to 352 ± 17 HV0.01 and the joints reached strength values up to 97 ± 7 MPa while the fracture area was always located at the ceramic interface in the HfO2 layer. Comparable joints, with AgCuTi3 as filler metal, brazed at 920 °C, only reached a shear strength of ~ 52 ± 2 MPa.

Keywords Vacuum brazing · High entropy alloy (HEA) · Eutectic high entropy alloy (EHEA) · Solid oxygen fuel cells · SOFC

1 Introduction

Conventionally, construction materials are based on one principal element or binary compound that is doped with small amounts of alloying elements in order to enhance the material properties. In this regard, most alloying elements that are used tend to form intermetallic phases when added in larger amounts. This can decrease, e.g., the shear strength, ductility, and corrosion resistance of the alloy [1]. Hence, fully assessed quaternary and quinary systems are rare, except for extrapolated CALPHAD-based diagrams. In this regard, Jien-Wei Yeh and Brian Cantor independently published their investigations on multicomponent alloys in 2004 [2, 3]. Cantor et al. smelted two alloys containing of 16, respectively 20 different elements in an equiatomic ratio, and observed the formation of a FCC-structured random solid solution, consisting of Cr, Co, Fe, Mn, and Ni in both specimens [2]. At the same time, Yeh et al. conducted investigations with a greater variety of different multicomponent alloys, whose microstructure featured only a few intermetallic phases. The lack of intermetallic phases within the microstructure led to the assumption that a high mixing entropy is responsible for the enhanced formation of random solid solutions [3].

In this regard, the thermodynamic stability of a phase at given environmental conditions is determined by the Gibbs energy, which depends on the enthalpy as well as the product of the entropy and temperature. While intermetallic phases feature, due to their stoichiometric composition, a low entropy, the forming enthalpy is rather high when compared with the enthalpy of solid solutions. The Gibbs energy of random solid solutions is dominated by the configurational entropy, which can be calculated with the following formula [4]:

Recommended for publication by Commission XVII - Brazing, Soldering and Diffusion Bonding

✉ L. Wojarski
Lukas.Wojarski@tu-dortmund.de

W. Tillmann
Wolfgang.Tillmann@tu-dortmund.de

D. Stangier
Dominic.Stangier@tu-dortmund.de

M. Manka
Matthias.Manka@tu-dortmund.de

C. Timmer
Christian.Timmer@tu-dortmund.de

[1] Institute of Materials Engineering, Faculty of Mechanical Engineering, TU Dortmund University, Leonhard-Euler-Str. 2, Dortmund, Germany

$$S = -R \cdot \Sigma x_i \cdot ln(x_i)$$

S is the configurational entropy, x_i the molar fraction of the element i, and R is the gas constant. This indicates that a maximization of the configurational entropy can be achieved by increasing the amount of elements added in an equimolar ratio. While taking this into consideration, the Gibbs energy of solid solutions can be higher than the energy of intermetallic phases, especially at high temperatures. This material derives its name from this effect [3]. HEAs are alloys with at least 5 elements with atomic percentage levels ranging from 5 to 35 according to the composition-based definition. Another definition of HEAs is based on the entropy level of the alloy, describing HEAs with an entropy above 1.5R, low entropy alloys as equal and below 1R, and medium entropy alloys as alloys with values in between the aforementioned values (Fig. 1) [3]. Some compounds defined as HEAs according to the compositional rule have an entropy lower than 1.5R; nonetheless, they are still considered to be a HEA.

The mechanical properties are mainly defined by the lattice in the solid solutions. While a FCC structure ensures a high ductility, yet lack a sufficient yield stress and hardness, a BCC structure shows the reverse properties. In order to combine the best features of both kinds of solid solutions, numerous research groups developed different types of EHEAs. In addition to the combination of a high ductility and hardness, the EHEAs have the advantage of an improved castability and an overall fine-grained structure [6–9]. Combining high yield stresses and ductility with a high resistance against corrosion and oxidation, even at high application temperatures, EHEAs are a potential sealant for solid oxygen fuel cells (SOFCs) [10, 11].

SOFCs commonly contain a solid oxide electrolyte such as yttria-stabilized zirconia (YSZ), which has to be adjoined to a metallic counterpart, e.g., Crofer 22 APU [12, 13]. Operating temperatures ranging between 500 and 1500 °C at ambient atmosphere demand a high resistance against oxidation on the one hand, and decent mechanical properties at elevated temperatures, on the other hand. Commonly, glass or glass-ceramic sealants, which can be adjusted to certain specific applications, are used. A disadvantage of these sealants is that they limit the SOFC in their applicable heating and cooling rate [14]. A potential alternative sealant for SOFCs might be

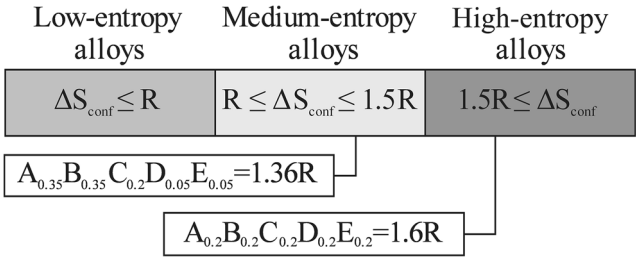

Fig. 1 Entropy-based definition [5]

the newly discovered EHEA $Nb_{0.73}CoCrFeNi_{2.1}$, which features a high oxidation resistance and increased ductility when compared with glass and glass-ceramic sealants.

This paper focuses on the applicability of $Nb_{0.73}CoCrFeNi_{2.1}$ as a filler metal or as a SOFC sealant. This study includes the production of the filler alloy, the characterization of the microstructure, and the determination of the shear strength of the joint.

2 Materials

The EHEA was smelted from pure elemental powders (Co, Cr, Fe, and Ni with a purity > 99.5 wt.-%) and a niobium foil (99.9 wt.-%). Cold-pressed as a pellet, the powder components were enfolded into the niobium foil. The smelting process was conducted in an arc furnace in an argon inert gas atmosphere. Every sample was molten 4 times to ensure a homogenous microstructure and chemical composition. The composition of the EHEA is listed in Table 1.

VDM® Crofer 22 APU (UNS S4 4535) steel was used for this process [15]. This ferritic steel was specifically developed by the ThyssenKrupp VDM GmbH for the use in SOFCs. It does not only suit the required oxidation resistance and thermal stress but, additionally, was adjusted to fit the thermal expansion coefficients of ceramics, which are typically used in SOFCs. It features a steel CTE between 10.3 and 12.7 mK^{-1} in the temperature range of 200 up to 1000 °C [15]. Table 2 lists the chemical composition of the Crofer 22 APU that was used as a steel substrate.

$20 \times 20 \times 2$ mm^3 coupons with a dimension of $20 \times 20 \times 2$ mm^3 were cut from steel plates and their surfaces were machined with a 1200 grit grinding paper. The interface was cleaned with ethanol prior to the brazing process. The employed yttria-stabilized zirconia had an yttria content of 3 mol.-% and features a CTE of 10.5 mK^{-1}, which corresponds to the CTE of the steel substrate [16] that was cut into coupons with $8 \times 8 \times 3$ mm^3 dimensions. In order to ensure the wettability of the ceramic, a metallization process with hafnium by means of arc PVD was conducted. For comparative purposes, additional brazements with a conventional 50-μm-thick AgCuTi3 brazing foil, manufactured by Umicore and referred to as CB4, were produced. The chemical composition of the braze is given in Table 3.

Table 1 Chemical composition of $Nb_{0.73}CoCrFeNi_{2.1}$ (wt.-%)

Nb	Co	Cr	Fe	Ni
19.0	16.5	14.5	15.6	34.4

Table 2 Chemical composition of Crofer 22 APU (wt.-%) [15]

Fe	C	Cr	Ti	La
Bal.	0.015	22.00	0.11	0.11

3 Experimental procedures

3.1 Brazing condition

The EHEA samples were cut into foils and whetted to ensure a homogeneous thickness of 300 μm. The foils were placed between both substrates with the steel counterpart at the bottom. The assembly was brazed in a vacuum furnace at a brazing temperature of 1200 °C. In order to avoid a strong diffusion and dissolution of the steel counterpart by the molten filler alloy, a high heating rate and short dwell time were applied. A heating rate of 50 K/min and an isothermal hold of 5 min at brazing temperature were chosen. The obtained vacuum reached $4.3 \cdot 10^{-4}$ mbar. A cooling rate of 50 K/min down to 900 °C was chosen. Subsequently, a 5 K/min cooling rate was applied until 500 °C, whereby the samples freely cooled down to room temperature. Thus, thermally induced stresses were reduced. In contrast, the conventional brazements using the conventional active brazing alloy were conducted at 920 °C in the same vacuum furnace with the same heating and cooling rates as for the EHEA joints.

3.2 Microstructural characterization

Cross-sections of the EHEA in the as-cast state, of the manufactured joints, as well as of the samples of the shear strength tests were metallographically prepared and examined using a scanning electron microscope (SEM) equipped with an energy dispersive X-ray spectroscope (EDS). It is noticeable that the accuracy of the EDS measurements for light elements like oxygen is low and therefore has to be critically scrutinized. The examination of the crystalline structure was conducted by XRD. To analyze the thermal stability of the braze synchrotron radiation at the DETLA (TU Dortmund University), BL9 was used, performing in situ X-ray diffraction. The samples were exposed to a photon energy of 20 keV ($\lambda = 0.062$ nm) before and after being heated up to a temperature of 900 °C under a graphite dome. The angle of incidence was set to 5° using a MAR345 plate detector with an exposure time of 300 s. Additionally, the joint was analyzed with the diffractometer Advanced D8 (Bruker AXS, Germany) using Cr-Kα radiation ($\lambda = 0.229$ nm) with an acceleration voltage of U = 40 kV and a current of I = 40 mA. The step size was set to $\Delta 2\Theta = 0.035°$ with an exposure time of 1 s. The 2Θ positions were calculated according to the lattice plane distance of the HEA $d = 2.0563$, 1.8043, and 1.2719 according to the results presented by Lu et al. [7]. Furthermore, CALPHAD calculations with Thermo-Calc were conducted in order to validate the XRD measurements and to identify possible intermetallic phases in the quinary alloy. Additionally, the microhardness of the as-cast state and the joint areas were measured as well.

Table 3 AgCuTi3 filler metal composition (wt.-%) [17]

Ag	Cu	Ti
Bal.	26.5	3

3.3 Joint fractography

In order to obtain the strength values and to evaluate the fracture behavior of the brazements, shear tests were performed with the apparatus illustrated in Fig. 2. The smaller YSZ coupon on top of the joint was fixed at the edge of the apparatus. By applying a force on the steel interconnect, it was pressed through the slot, which was adjusted to the dimensions of the joint samples. The average shear strength was calculated as a mean value from three samples as the quotient of the obtained ultimate shear strengths divided by the brazed area. Finally, cross-sections of the reassembled fractured samples were prepared to identify the fracture path and failure mechanisms.

4 Results and discussion

In order to estimate and predict the constituents in the EHEA in dependence of the temperature, simulations with Thermo-Calc, using the TCHEA2 database, were performed. Figure 3 shows the phase fraction diagram of the EHEA $Nb_{0.73}CoCrFeNi_{2.1}$. The melting range is assumed to be 1245 to 1274 °C. The smelt solidifies by forming a face-centered cubic solid solution (3. FCC_L12) and a hexagonal

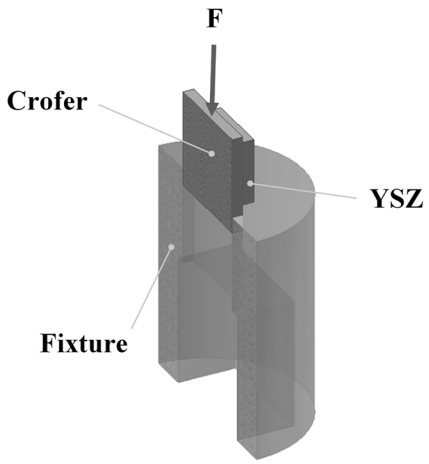

Fig. 2 Schematic illustration of the shear strength test device in a profile view

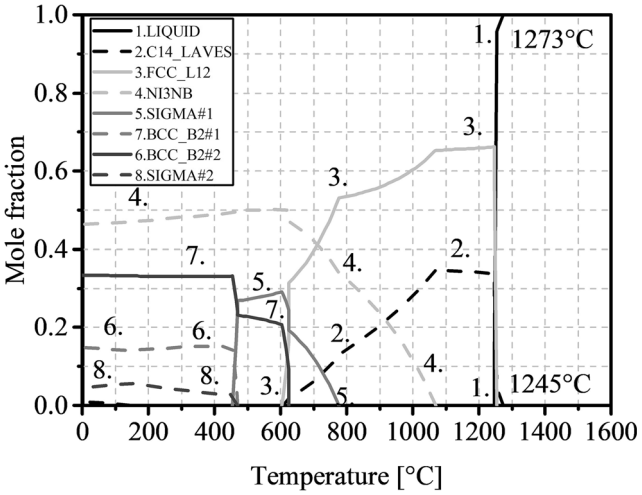

Fig. 3 Phase fraction diagram of the EHEA $Nb_{0.73}CoCrFeNi_{2.1}$

C14-type Laves phase (2. C14_LAVES). In the equilibrium state, additional intermetallic phases and solid solutions form at temperatures below 1100 °C. Therefore, comparably high cooling rates are necessary to avoid the formation of intermetallic phases. The chemical composition of these phases, based on the simulation, is summarized in Table 4.

4.1 Microstructure of the filler metal

In accordance with the findings of Lu et al., the microstructure of the $Nb_{0.73}CoCrFeNi_{2.1}$ alloy consists of two fine-grained phases. Figure 4 shows a backscattered electron image (BSE) of the alloy after smelting. According to the predicted compositions in Table 4, the Laves phase has a higher niobium content than the FCC-structured solid solution (see Table 5). Since niobium is the element with the highest atomic weight within this alloy, the bright phase has to be a niobium-rich Laves phase. By implication, the dark phase contains less niobium and hence is the solid solution.

Table 4 Chemical composition of the phases in Fig. 3 at the given temperatures (wt.-%)

Phase	T	Elements (wt.-%)				
(–)	[°C]	Nb	Co	Cr	Fe	Ni
C14_ LAVES	1100 °C	36.2	16.1	12.1	14.4	21.2
FCC_L12	1100 °C	7.6	18.0	17.9	19.2	37.4
NI3TA_D0A	800 °C	34.0	6.5	1.3	2.9	55.3
SIGMA#1	600 °C	0.8	20.2	48.0	18.9	12.0
BCC_B2#2	500 °C	0.1	15.8	56.7	21.5	6.1
BCC_B1#1	300 °C	–	38.4	5.6	49.0	7.2
SIGMA#2	300 °C	20.7	32.9	46.4	–	–

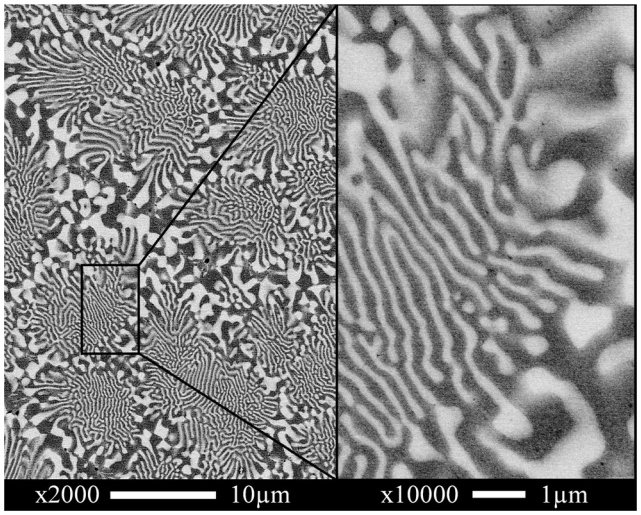

Fig. 4 Microstructure of a $Nb_{0.73}CoCrFeNi_{2.1}$ sample

The average chemical compositions of the two constituents of the braze alloy measured by EDS are given in Table 5. The average values were calculated from three samples and 10 measurements per sample and phase. The resulting average microhardness of the alloy, which was also calculated from 30 measurements, was 525 ± 50 HV0.01. The comparably high hardness value can be attributed to the short cooling time after smelting, which leads to a very fine microstructure and high distortion of the lattice.

X-Ray diffraction was performed in order to verify the phases identified by SEM and the CALPHAD calculations on the one hand, and to investigate whether the chosen brazing cycle leads to the generation of intermetallic phases according to Fig. 3 on the other hand. In this regard, Fig. 5 features the XRD patterns of the EHEA filler alloy at room temperature and at 900 °C in the as-casted state and after a simulated brazing cycle at 1200 °C. All diffractograms possess the characteristic peaks of the FCC solid solution and of the Laves phase. Besides these constituents of the microstructure, only a graphite peak could be identified, which can be attributed to the graphite dome in which the samples were placed during the measurements. Hence, no tendency of the alloy to form intermetallic phases could be observed within these investigations.

While the BSE image and the EDS analysis confirm the prediction of the formation of two high temperature phases within the calculated phase fraction diagram (Fig. 2), the measured melting range appears to be significantly lower when

Table 5 Average chemical composition of the EHEA samples (wt.-%)

Phase	Nb	Co	Cr	Fe	Ni
Laves	36.4	14.2	10.0	12.7	26.7
FCC	10.2	16.4	17.4	21.3	34.7

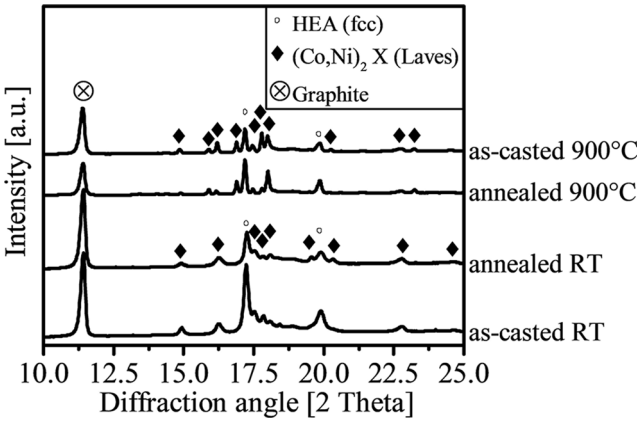

Fig. 5 XRD patterns of the EHEA alloy in the as-casted and annealed state at room temperature and at 900 °C

compared with the calculations (see Fig. 6). The differential thermal analysis revealed a melting range from 1170 to 1222 °C, which is about 50 °C lower compared with the predicted values. As mentioned above, the brazing temperature was set to 1200 °C as the alloy is mainly in a liquid state and strong diffusion as well as base material dissolution is expected at such high temperatures.

4.2 Microstructure of the $Nb_{0.73}CoCrFeNi_{2.1}$ joints

A sound joint without pores or voids was manufactured using $Nb_{0.73}CoCrFeNi_{2.1}$ as a filler material as shown in Fig. 7. The white reaction layer, which has formed at the interface between the yttria-stabilized zirconia and the filler material, is, according to its chemical composition, listed in Table 6, most probably hafnium dioxide (HfO_2). Furthermore, the overall microstructure of the filler metal is coarser when compared with the microstructure of the ingots in the as-cast state. But the eutectic microstructure consisting of two constituents still remained unchanged.

Comparing the chemical compositions of the as-cast state in Table 5 with the phase compositions in Table 6, it is obvious that the compositions of the single constituents have

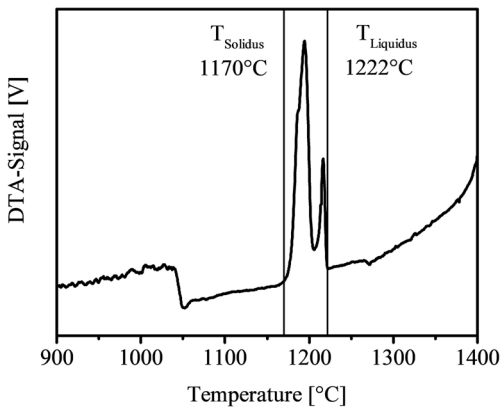

Fig. 6 DTA curve of the $Nb_{0.73}CoCrFeNi_{2.1}$ [18]

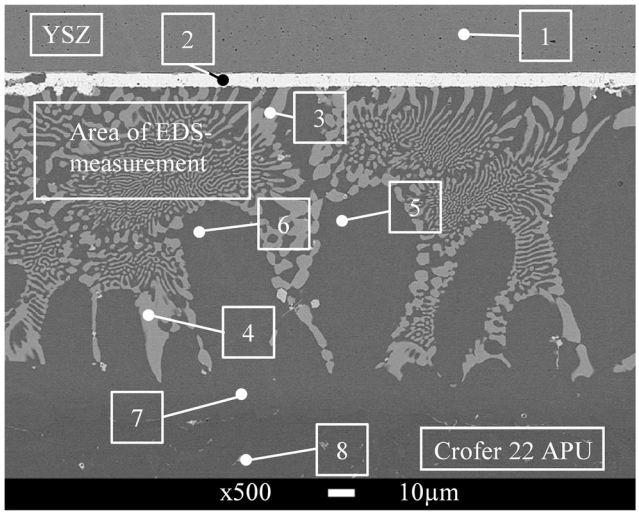

Fig. 7 YSZ-Crofer sample with a $Nb_{0.73}CoCrFeNi_{2.1}$ filler metal

changed significantly. The dark phase at points 5 and 6 does not contain any niobium, the nickel and cobalt contents are reduced, while the chromium content increased, and the iron content rose significantly. Points 3 and 4 in the brighter phase feature a slightly increased niobium content, as well as a small hafnium content. Only the chromium content remained stable, while the cobalt and nickel contents decreased and the iron content increased. The microhardness measurements of the joints revealed a mean hardness value of only 369 ± 17 HV0.01. The lower value compared with the as-cast state can be explained with the slower cooling and the resulting coarser grain structure in addition to the change in the chemical composition.

The interface of the ceramic substrate still clearly exists and no elements of the filler metal could be detected above the white reaction layer. However, at the steel interface, a consistent transition from the filler metal to the steel substrate could be observed. In order to identify the average composition of the alloy formed in the brazing area, an area scan was

Table 6 Chemical composition of the EDS point analysis in Fig. 7 (wt.-%)

No.	O	Cr	Fe	Co	Ni	Zr	Nb	Hf
1	24.3	–	–	–	–	74.2	–	1.4
2	14.5	–	0.9	–	–	–	–	84.6
3	–	10.5	29.7	6.5	12.0	–	38.0	3.3
4	–	10.3	31.9	5.9	10.1	–	39.8	2.0
5	–	20.2	56.3	7.5	16.0	–	–	–
6	–	20.6	56.0	7.6	15.8	–	–	–
7	–	19.8	67.6	3.9	8.7	–	–	–
8	–	26.0	70.5	–	3.5	–	–	–

Table 7 Composition of the eutectic area measurement formed in the brazing seam (wt.-%)

Nb	Co	Cr	Fe	Ni
18.0	6.7	16.7	43.9	14.7

conducted by means of EDS as shown in Fig. 7 and the composition of the obtained alloy is summarized in Table 7.

Due to the change in the composition of the phases formed in the brazing area in comparison with the braze alloy in an as-cast condition, CALPHAD calculations were repeated based on the measured alloy composition obtained from the area scan in order to identify the generated phases in the microstructure of the joint. The phase fraction diagram, calculated with Thermo-Calc 2017b and the TCHEA2 database, shows that the melting range of alloys formed in the brazing seam increased. While the solidus temperature only increased by 50 K, the liquidus temperature increased by almost 200 K. But according to the CALPHAD calculations, the microstructure of the joints still consists of the FCC solid solution and the Laves phase, even though the chemical composition of the constituents has changed significantly (Fig. 8).

Additionally, XRD measurements of the brazed samples were conducted after the steel counterpart was almost completely removed by grinding (Fig. 9). The XRD patterns of the brazed alloy on the ceramic counterpart reveal that besides zirconia, iron, and hafnium as well as HfO_2, the FCC-structured solid solution and the Laves phase could be determined. They were already identified with the CALPHAD simulations, based on the actual composition of the brazed alloy.

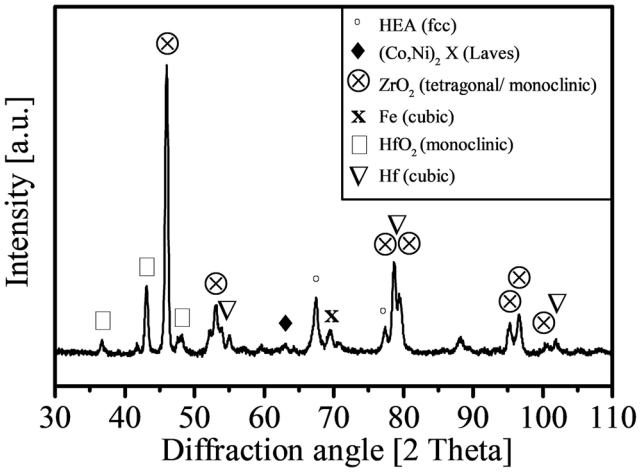

Fig. 9 Phase fraction diagram of the brazed sample after removal of the Crofer substrate by polishing (YSZ at the bottom)

4.3 AgCuTi3 joint microstructure

The microstructure of the joint brazed with the conventional filler alloy is shown in Fig. 10. The filler alloy shows a good connection to both substrates and no distinct diffusion between the YSZ ceramic and the braze alloy (see Table 8 point 1) could be observed, while the interface between the steel substrate and the filler alloy shows a slight erosion.

Four different phases formed in the brazing seam. The bright white phase (points 2 and 3) mainly contains silver with some oxygen and iron as a result of diffusion processes between the ceramic and the steel substrate. The grayish phases in points 4 and 5 mainly consist of copper with small amounts of iron, copper, and titanium. The dark gray phase (see no. 6) is an iron-chromium-based phase, into which small amounts of titanium are dissolved. Finally, the dark vast distributed black spherical phases are most probably TiO_2 phases, which

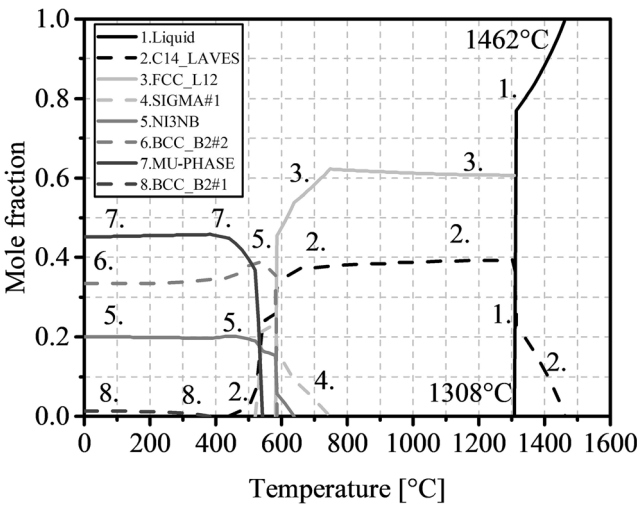

Fig. 8 Phase fraction diagram of the alloy described in Table 6

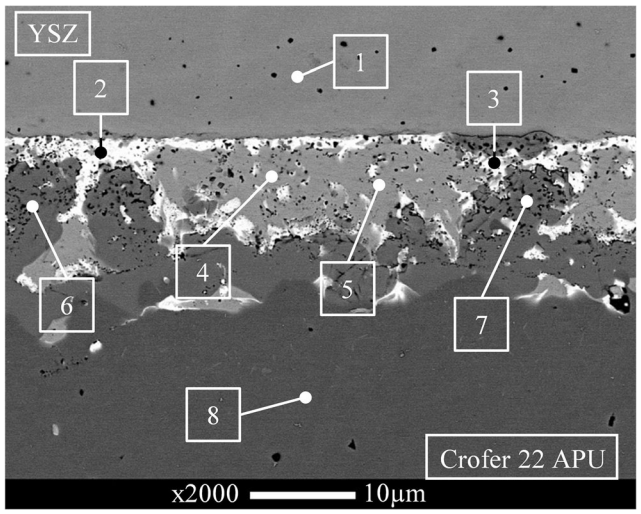

Fig. 10 YSZ-Crofer joint microstructure with AgCuTi3 as filler metal

Table 8 Chemical composition of the EDS point analysis in Fig. 10(wt.-%)

No.	Ag	Cu	Ti	Fe	Cr	Zr	O
1	–	–	–	–	–	72.3	27.3
2	85.6	3.3	4.7	0.7	–	–	5.7
3	90.9	4.2	1.3	0.5	–	–	3.1
4	4.7	92.3	2.1	0.9	–	–	–
5	6.5	91.8	0.4	1.3	–	–	–
6	–	1.9	12.1	67.9	18.1	–	–
7	2.0	3.1	22.1	46.9	14.1		11.8
8	–	1.2	1.7	74.6	22.5	–	–

appear to be dark in the BSE mode due to their comparably low atomic weight (see no. 7).

4.4 Mechanical properties

The average shear strength of the samples brazed with $Nb_{0.73}CoCrFeNi_{2.1}$ was 97 ± 7 MPa, while the conventionally brazed samples with AgCuTi3 as filler alloy reached only 52 ± 2 MPa. As shown in Fig. 11, the fracture propagated predominantly in the hafnium-dioxide reaction layer. On the steel side, the eutectic phase mixture is almost completely intact, while the fracture appeared solely in the reaction layer. The brighter niobium-enriched phase, identified before as the C14 Laves phase, close to the reaction layer, features a few cracks that can be attributed to the high shear stresses during loading in combination with a brittle material behavior of the Laves phase. On the contrary, the surrounding FCC phase is free of cracks. Hence, the hafnium-dioxide reaction limits the joint strength, whereas the full potential of $Nb_{0.73}CoCrFeNi_{2.1}$ as a SOFC sealant is not completely exploited.

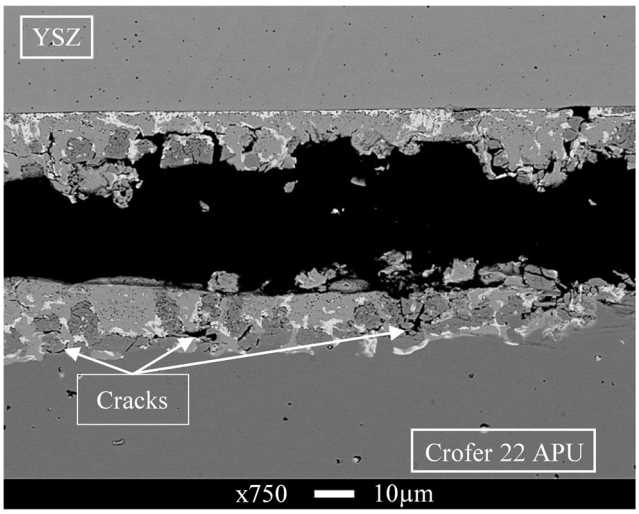

Fig. 11 Fractured YSZ-EHEA-Crofer sample

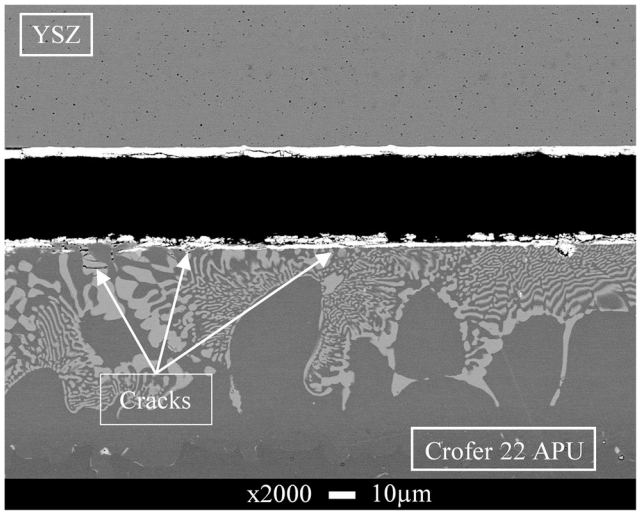

Fig. 12 Fractured YSZ-AgCuTi3-Crofer sample

The fracture of the samples brazed with the AgCuTi3 filler alloy differs from that of the $Nb_{0.73}CoCrFeNi_{2.1}$-brazed samples. The joints failed close to the center of the brazing seam (see Fig. 12).

5 Conclusion

This research revealed that eutectic high-entropy alloys are applicable as high temperature filler metals tor seal materials in SOFCs. Sound joints could be obtained for Crofer 22 APU and hafnium-metallized YSZ bonds by using $Nb_{0.73}CoCrFeNi_{2.1}$ as a filler metal. A fine-grained eutectic microstructure, comprising a FCC solid solution and a C14 Laves phase, was identified in the as-cast state of the EHEA, which could be retained with a growth of the grain structure after brazing. No additional intermetallic phase was formed in the brazing seam, only the desired hafnium-dioxide reaction layer developed at the ceramic interface. Diffusion processes between the filler metal $Nb_{0.73}CoCrFeNi_{2.1}$ and the steel substrate Crofer 22 APU led to changes in the chemical composition of the constituents in the brazing seam. The EHEA joints featured an average shear strength of 97 ± 7 MPa, while brazements with AgCuTi3 only reached 52 ± 2 MPa. Even with a ~2 times higher shear strength, the full potential of the EHEA filler was not completely achieved, due to restrictions caused by the hafnium metallization. Besides a few cracks in the Laves phase close to the fracture mirror, the sheared surface was located solely in the hafnium-dioxide reaction layer. Therefore, further investigations are required in order to optimize the metallization thickness or material to fully exploit the potential of the $Nb_{0.73}CoCrFeNi_{2.1}$ alloy.

Acknowledgments Open Access funding provided by Projekt DEAL. The authors gratefully acknowledge the DELTA machine group for

providing synchrotron radiation within BL and Dr. Iris-Aya Laemmerhirt for the linguistic.

References

1. Hornbogen E., et al.: Metalle. Springer Berlin Heidelberg 2016, ISBN: 103-540-34010-6
2. Cantor B, Chang ITH, Knight P, Vincent AJB (2004) Microstructural development in equiatomic multicomponent alloys. Mater Sci Eng A 375–377:213–218
3. Yeh J.-W., et al.: Nanostructured high-entropy alloys with multiple principal elements: novel alloy design concepts and outcomes. Advanced Engineering Materials 2004, 6, No.5 p. 299–303
4. Porter DA, Easterling KE (1992) Phase transformations in metals and alloys. Chapman & Hall ISBN 978-0-442-31638-9
5. Yeh J.-W.: Alloy design strategies and future trends in high-entropy alloys. JOM 65 (12) p. 1759-1771
6. Lu Y., Dong Y. et al.: A promising new class of high-temperature alloys: eutectic high-entropy alloys. Scientific reports 4:6200
7. Lu Y, Jiang H, Guo S, Wang T, Cao Z, Li T (2017) A new strategy to design eutectic high-entropy alloys using mixing enthalpy. Intermetallics Vol 91:124–128
8. Huo W, Zhou H (2018) Microstructure and properties of novel CoCrFeNiTax eutectic high-entropy alloys. J Alloys Compd 735: 897–904
9. Wani I., Bhattacharjee T.: Ultrafine-grained AlCoCrFeNi 2.1 eutectic high-entropy alloy. Materials Research Letters 4 (3), p. 174–179
10. Raphel A., Kumaran S., et al.: Oxidation and corrosion resistance of AlCoCrFeTi high entropy alloy. Materials Today: Proceedings 4 (2) p. 195–202
11. Kai W., Cheng F.P., et al.: The oxidation behavior of the quinary FeCoNiCrSix high-entropy alloys. Materials Chemistry and Physics 2010 p. 362–369
12. Kendall K., Kendall M.: High-temperature solid oxide fuel cells. Elsevier 2015, ISBN: 103-540-34010-6, p. 1–24
13. Rodríguez-López S, Comesana R et al (2015) Laser cladding of glass-ceramic sealants for SOFC. J Eur Ceram Soc 35(210):4475–4484
14. Jeffrey WF (2005) Sealants for solid oxide fuel cells. J Power Sources 147:46–57
15. VDM-Metals GmbH "VDM® Crofer 22 APU" , data sheet, received: 14.09.2018, 11:01 GMT+1
16. MicroCeram, MC-Flyer, "Hochleistungskeramik", received 26.05.2020; 16:50 GMT+1
17. SAXONIA Technical materials GmbH "CB4", data sheet, received: 14.09.2018, 11:03 GMT+1
18. Tillmann W., Wojarski L., et al.: Eutectic high entropy alloys – a novel class of materials for brazing applications